A DIRECT IMAGING ALGORITHM FOR EXTENDED TARGETS

SONGMING HOU [*], KNUT SOLNA [†], AND HONGKAI ZHAO [‡]

Abstract. We present a direct imaging algorithm for extended targets. The algorithm is based on a physical factorization of the response matrix of a transducer array and the Multi-Signal Classification (MUSIC) imaging function is used to visualize the results. A resolution and noise level based thresholding strategy is developed for regularization. The algorithm is simple and efficient since no forward solver or iteration is needed. Multiple-frequency information improves both resolution and stability of the algorithm. Efficiency and robustness of the algorithm with respect to measurement noise and random medium fluctuations are demonstrated.

Keywords: Helmholtz equation, singular value decomposition, time reversal, response matrix, boundary integral equation

1. Introduction. Probing a medium using waves to detect and image targets has many applications. The objective is to infer the location and/or geometry of targets from the scattered wave field. Examples include ultrasound imaging in medical applications, detection of defects in nondestructive testing, underground mine detection and target detection using radar or a sonar system. In the general inverse problem approach the whole medium is regarded as the unknown. Hence, an inverse or pseudo-inverse of the forward operator has to be approximated and computed. The inverse problem is often nonlinear even if the forward problem is linear. A nonlinear optimization problem typically needs to be solved via iterations. This optimization problem usually involves solving an adjoint forward problem at each iteration. Moreover, the inverse problem is often ill-posed and regularization has to be introduced. As a consequence, imaging the whole medium using this general inverse problem approach may be too complicated and too expensive to be practical in many applications, for instance if the imaging domain is large. If the background medium is homogeneous and some simple boundary condition is satisfied at the boundary of the target, the inverse problem can be turned into a geometric problem, that is, the problem of determining the shape of the target from the scattered wave field pattern. In this case the 'number of degrees of freedom' is greatly reduced from the case of imaging the whole medium. If incident plane waves and the corresponding far field patterns are used this is the classical 'inverse scattering problem'. This problem involves a nonlinear optimization problem with respect to an appropriate shape space which is typically solved using shape derivatives via iterations. Again shape regularization is needed and an adjoint forward problem has to be solved to find the shape derivative in each iteration.

Here we propose a direct imaging algorithm to image both location and geometry of extended targets. The motivation for our method is to locate or visualize dominant scattering events for the scattered wave field. In homogeneous media this is equivalent

---

[*]Dept of Math, MSU, East Lansing, MI, 48824, mickey@math.msu.edu
[†]Dept of Math, UCI, Irvine, CA, 92697, ksolna@math.uci.edu
[‡]Dept of Math, UCI, Irvine, CA, 92697, zhao@math.uci.edu

to finding the boundary of a target that has some contrast from the background. For heterogeneous media, whether we can clearly locate or visualize the boundary depends on two factors: (1) to what extent the scattering at the boundary of the target dominates other scattering events in the medium, e.g., the signal to noise ratio; (2) knowledge about the background medium known, e.g., how well the Greens function for the background medium can be approximated. With a physically based thresholding we show that our direct imaging algorithm can deal with quite strong measurement noise and also some random heterogeneities in the medium.

Our physical model is the Helmholtz equation for harmonic waves. An array of transducers that can send out waves and record scattered waves is used to probe the medium. The measurement data is the response matrix, which are the inter-element responses of the array, i.e., the recorded signal at a receiver corresponding to a probing pulse sent out by a transmitter. This matrix gives all the information about the medium that can be obtained with the transducer array. Based on a physical factorization of the scattered field we characterize the Singular Value Decomposition (SVD) of the response matrix for extended targets. We then design a direct imaging function based on the SVD and introduce a thresholding strategy for regularization based on the physical resolution of the array and the noise level.

A physical motivation for our algorithm is that strong scattering events can be considered as sources for the scattered field. This is related to the idea behind the physical experiment of time reversal. In time reversal the received wave field is time reversed and back propagated into the medium. The retransmitted wave will focus on sources. For target detection, the target is illuminated by a probing wave first and then the time reversed wave will focus on dominant scatterers. This procedure can also be repeated, i.e., iterated time reversal. However, the standard time reversal procedure only provides a way to locate the most dominant scattering event associated with the largest singular value or dominant events associated with different singular values one by one. To image an extended target we need to use the SVD to extract dominant events that characterize the shape information.

Our imaging function is of a similar form as the MUltiple SIgnal Classification (MUSIC) imaging function. The previous MUSIC algorithm [25, 9, 15, 23, 12, 10] can only locate small targets. Under the assumption of point targets the response matrix has a simple structure. This structure is used in MUSIC and has also been exploited to focus a wave field on selected scatterers using iterated time reversal [24, 22, 20, 21, 14, 19]. The iterated time reversal procedure corresponds to the power method for finding the dominant singular vectors for the response matrix. However, with the point target assumption, physical properties and the geometry of the target are neglected. More importantly an extended target is not a superposition of point targets. For extended targets the response matrix has a more complicated structure and we exploit this structure in our approach. Two key ideas behind our algorithm are: (1) a physical representation of the scattered field and the corresponding response matrix; (2) a thresholding strategy based on the resolution of the array and the SVD of the response matrix. We use these two ideas to extract important contributions to the scattered field simultaneously from the SVD of the response matrix. Moreover our imaging algorithm can (1) incorporate physical properties of the targets into the imaging function; (2) use different wave form, e.g., point source or plane wave, for illumination; (3) use data in near or far field.

This algorithm is different from the one proposed in [13], in which a shape optimization is used to match all measurements in the response matrix. The method can

be parallelized easily since the evaluation of the imaging function at different grids are independent.

The linear sampling method, first proposed in [8], is also a direct imaging algorithm for the inverse scattering problem. The method is based on a characterization of the range of the scattering operator for the far field pattern. It is shown that the far field pattern of a point source located inside the object should be in the range of the scattering operator. Kirsch gave a factorization of the scattering operator [16] and use this factorization for imaging. The relation between the MUSIC and the linear sampling method is studied in [7, 17]. The approach presented here differ from the linear sampling method. First, our algorithm is based on a different factorization. Second we use a physically based thresholding instead of the Tikhonov regularization in the linear sampling method. Moreover, our targets can be illuminated either by point sources or by incoming plane waves and our data can be near or far field.

The outline of the paper is as follows. In section 2 we first give a brief discussion of the response matrix and its SVD for point targets. We present a study of the response matrix for extended targets and develop our image algorithm in Section 3. We develop a resolution analysis and a noise level based thresholding in section 4. Extensive numerical experiments are presented in Section 5 to demonstrate our imaging algorithm.

2. The Response Matrix And Its Singular Value Decomposition for point targets. Our setup uses an array of transducers that can send and receive signals to probe the medium. For simplicity we mainly focus on the case with an active array, i.e., the transducers can both send out and record signals. These results can easily be extended to arrays where transmitters and receivers are different, which will be discussed briefly at the end of this section. The scalar wave equation, e.g. for acoustic waves, is used to describe the wave field. Figure 2.1 shows a typical configuration. We surround the region of interest with transducers, giving a full aperture. The background medium could be either homogeneous or weakly heterogeneous and random. There could be one or more targets in the region.

Define the interelement response $P_{ij}(t)$ to be the signal received at the $j-th$ transducer with an impulse sent out from the $i-th$ transducer. For an array consisting of N transducers, the matrix $P(t) = [p_{ij}(t)]_{N \times N}$ is called the response matrix. Since the medium is static we have $P_{ij}(t) = P_{ji}(t)$ due to spatial reciprocity. For a source signal distribution $\vec{e}(t) = [e_1(t), e_2(t), \ldots, e_N(t)]^T$, where $e_i(t)$ is the output signal at the $i-th$ transducer and T is transpose, the reflected signal at the array is,

$$\vec{r}(t) = [r_1(t), r_2(t), \ldots, r_N(t)]^T = P(t) * \vec{e}(t),$$

with $*$ denoting convolution in time. In the frequency domain we have

$$\hat{\vec{r}}(\omega) = \hat{P}(\omega)\hat{\vec{e}}(\omega),$$

where ω is the frequency and $\hat{P}(\omega)$ is the Fourier transform of $P(t)$. In this paper, we focus on a frequency domain formulation with time harmonic waves. We briefly review the basic structure of the response matrix $\hat{P}(\omega)$ for a fixed frequency and omit the ^notation below. Denote the Greens function of the homogeneous background at a particular frequency by $G^0(\boldsymbol{\xi}, \boldsymbol{x})$. Due to the spatial reciprocity, $G^0(\boldsymbol{x}, \boldsymbol{\xi}) = G^0(\boldsymbol{\xi}, \boldsymbol{x})$. Here we also suppress the dependence of the Greens function on the frequency when there is no confusion. Assume that there are M point scatterers located at $\boldsymbol{x}_1, \boldsymbol{x}_2, \ldots, \boldsymbol{x}_M$ in the medium with reflectivity $\tau_1, \tau_2, \ldots, \tau_M$, if we neglect the multiple scattering
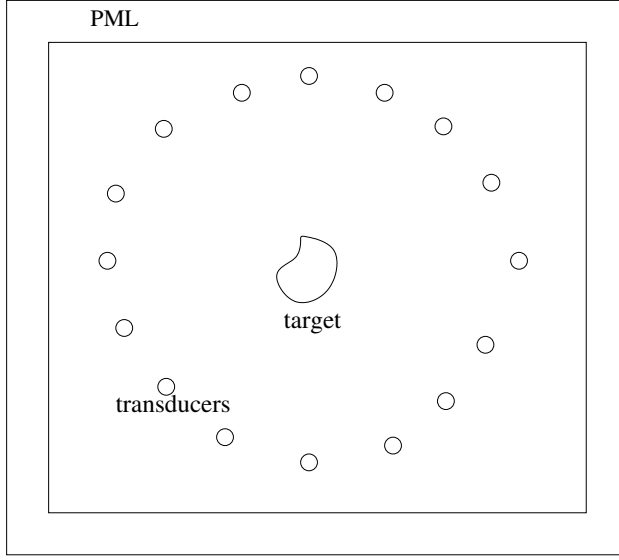
3

FIG. 2.1. *Setup for Imaging Experiments*

among the scatterers, then for a signal $\vec{e}(\omega) = [e_1(\omega), e_2(\omega), \ldots, e_N(\omega)]^T$ sent out from the active array, the reflected signal at the $j - th$ transducer is

$$r_j(\omega) = \sum_{k=1}^{M} \sum_{i=1}^{N} G^0(\boldsymbol{\xi}_j, \boldsymbol{x}_k) \tau_k G^0(\boldsymbol{\xi}_i, \boldsymbol{x}_k) e_i(\omega),$$

where $\boldsymbol{\xi}_1, \boldsymbol{\xi}_2, \ldots, \boldsymbol{\xi}_N$ are the locations of the transducers. If we define the illumination vectors, $\vec{g}_k^0, k = 1, 2, \ldots, M$, to be

$$\vec{g}_k^0 = [G^0(\boldsymbol{\xi}_1, \boldsymbol{x}_k), G^0(\boldsymbol{\xi}_2, \boldsymbol{x}_k), \ldots, G^0(\boldsymbol{\xi}_N, \boldsymbol{x}_k)]^T,$$

i.e., the wave field at the array of transducers corresponding to a point source at the $k - th$ scatterer, we have

$$P(\omega) = \sum_{k=1}^{M} \tau_k \vec{g}_k^0 \vec{g}_k^{0T} \quad \text{and} \quad \vec{r}(\omega) = P(\omega)\vec{e}(\omega). \tag{2.1}$$

Due to the spatial reciprocity $P(\omega)$ is symmetric. The 'time reversal step' corresponds to a phase conjugation in the frequency domain, and we form $R(\omega) = \overline{P(\omega)}P(\omega) = P^*(\omega)P(\omega)$ which is called the time reversal matrix (operator) where $*$ denotes the adjoint. It is shown that the time reversal operator is an optimal spatial and temporal matched filter in [26, 5]. The matrix $R(\omega)$ is Hermitian and from (2.1) we have

$$R(\omega) = \sum_{k=1}^{M} \overline{\tau_k \vec{g}_k^0 \vec{g}_k^{0T}} \sum_{k'=1}^{M} \tau_{k'} \vec{g}_{k'}^0 \vec{g}_{k'}^{0T} = \sum_{k'=1}^{M} \sum_{k=1}^{M} \Lambda_{k,k'} \vec{g}_k^0 \vec{g}_{k'}^{0T}, \tag{2.2}$$

where

$$\Lambda_{k,k'} = \overline{\tau}_k \tau_{k'} < \vec{g}_k^0, \vec{g}_{k'}^0 > = \overline{\tau}_k \tau_{k'} \overline{\vec{g}_k^0}^T \vec{g}_{k'}^0.$$

4

Using the representations (2.1) and (2.2) we can easily see that both the response matrix $P(\omega)$ and the time reversal matrix $R(\omega)$ are of rank M, i.e., the number of scatterers, and that their range is the span of the illumination vectors $\vec{g}_k^0, k = 1, 2, \ldots, M$. Define the point spread function

$$\Gamma(\boldsymbol{x}', \boldsymbol{x}) = \sum_{i=1}^{N} \overline{G^0(\boldsymbol{\xi}_i, \boldsymbol{x}')} G^0(\boldsymbol{\xi}_i, \boldsymbol{x}). \tag{2.3}$$

Then $\Gamma(\boldsymbol{x}', \boldsymbol{x})$ is exactly the wave field at point $\boldsymbol{x}$ after phase conjugating the signal received at the active array for a point source at $\boldsymbol{x}'$ and sending it back into the medium. The support of the point spread function also defines the resolution of the array. That the scatterers are well resolved by the active array means

$$\Gamma(\boldsymbol{x}_k, \boldsymbol{x}_{k'}) = \overline{\vec{g}_k^0}^T \vec{g}_{k'}^0 \approx 0 \text{ if } k \neq k'$$

i.e., the wave field corresponding to the time reversal of a point source at one scatterer is almost zero at all other scatterers. In the well resolved case $\vec{g}_k^0$ $(\overline{\vec{g}_k^0})$ is the left (right) singular vectors for $P(\omega)$ with singular values $\tau_k \|\vec{g}_k^0\|^2$ since

$$P(w)\overline{\vec{g}_k^0} = \tau_k \|\vec{g}_k^0\|^2 \vec{g}_k^0, \quad P^*(w)\vec{g}_k^0 = \tau_k \|\vec{g}_k^0\|^2 \overline{\vec{g}_k^0}. \tag{2.4}$$

It is shown in [12] how multiple scattering among several point scatterers can be taken into account. Similar to the Lippmann-Schwinger formula, the response matrix can be written as

$$P(\omega) = \sum_{k=1}^{M} \tau_k \vec{g}_k^0 \vec{g}_k^T, \tag{2.5}$$

where $\vec{g}_k^0$ is the illumination vector for the homogeneous background medium and $\vec{g}_k$ is the illumination vector for the medium that includes all point scatterers. Hence, the column space of the response matrix (spanned by the left singular vectors) is still the same as in the case with a **homogeneous background**, i.e., spanned by $\vec{g}_k^0, k = 1, 2, \ldots, N$. The structure of the response matrix (2.5) can be used to image the locations of the point scatterers. In the MUSIC algorithm one of the crucial steps is the definition of the **signal space** V^S in terms of the SVD of the response matrix. The noise space V^N is the orthogonal complement of V^S. Denote $\vec{g^0}(\boldsymbol{x})$ to be the illumination vector at a searching point $\boldsymbol{x}$, then the imaging function is constructed as

$$I(\boldsymbol{x}) = \frac{1}{\|P_{V^N} \vec{g^0}(\boldsymbol{x})\|^2}, \qquad \text{where } P_{V^N} \text{ is the projection operator.} \tag{2.6}$$

For the ideal point scatterer case, the signal space is spanned by the singular vectors corresponding to non-zero singular values. From the structure of the response matrix (2.5) it is easy to see that $I(\boldsymbol{x})$ becomes large when $\boldsymbol{x}$ matches the location of one of the scatterers. It is also easy to see that we can not have more scatterers than transducers (since the response matrix will have a full rank) for the MUSIC imaging function. A nice property of the projection operation is that we do not need a one to one correspondence between the singular vector and the illumination vector of the

5

scatterers. Let $\vec{u}_1, \vec{u}_2, \ldots, \vec{u}_N$ be the set of singular vectors that span the signal space V^S. The imaging function for MUSIC is defined by

$$I(\boldsymbol{x}) = \frac{1}{\|\vec{g}^0(x)\|^2 - \|P_{V^S}\vec{g}^0(x)\|^2} = \frac{1}{\|\vec{g}^0(x)\|^2 - \sum_{k=1}^{N} |\,\vec{g}^0(x) \cdot \vec{u_k}\,|^2}.$$

Remark: If the array is composed of two different sets of transmitters and receivers, e.g., there are s transmitters located at $\boldsymbol{\xi}_1, \ldots, \boldsymbol{\xi}_s$ and there are r receivers located at $\boldsymbol{\eta}_1, \ldots, \boldsymbol{\eta}_r$. The response matrix for M point targets located at $\boldsymbol{x}_1, \ldots, \boldsymbol{x}_M$ with reflectivity $\tau_1, \ldots, \tau_M$ becomes

$$P(\omega) = \sum_{k=1}^{M} \tau_k \vec{g_k^s} \vec{g_k^r}^T, \tag{2.7}$$

where

$$\vec{g_k^r} = [G^0(\boldsymbol{\eta}_1, \boldsymbol{x}_k), G^0(\boldsymbol{\eta}_2, \boldsymbol{x}_k), \ldots, G^0(\boldsymbol{\eta}_r, \boldsymbol{x}_k)]^T,$$

and

$$\vec{g_k^s} = [G^0(\boldsymbol{\xi}_1, \boldsymbol{x}_k), G^0(\boldsymbol{\xi}_2, \boldsymbol{x}_k), \ldots, G^0(\boldsymbol{\xi}_s, \boldsymbol{x}_k)]^T$$

$k = 1, 2, \ldots, M$, are illumination vectors for the receiver and transmitter arrays respectively. The response matrix is of rank M. If the targets are well resolved by the transmitter and receiver array, $\vec{g_k^s}$ and $\vec{g_k^r}$ are the left and right singular vectors for the response matrix $P(\omega)$ respectively. In general, $\vec{g_k^s}$ and $\vec{g_k^r}$, $k = 1, 2, \ldots, M$, span the column and row signal spaces, V_C^S and V_R^S, respectively. The MUSIC imaging function can be constructed using both of them. For example, let $\vec{g}_s^0(\boldsymbol{x})$ and $\vec{g}_r^0(\boldsymbol{x})$ be the illumination vector at a searching point $\boldsymbol{x}$ corresponding to the transmitter and receiver arrays respectively, we define the imaging function

$$I(\boldsymbol{x}) = \frac{1}{\|\vec{g}_s^0(x)\|^2 - \|P_{V_C^S}\vec{g}_s^0(x)\|^2} + \frac{1}{\|\vec{g}_r^0(x)\|^2 - \|P_{V_R^S}\vec{g}_r^0(x)\|^2}$$

For extended scatterers whose sizes are comparable to or larger than the resolution of the array the above analysis is not valid anymore. The response matrix has a more complicated structures. Even for a single extended scatterer, there will be many non-zero singular values. For example, it was shown in [6] that compressibility contrast and density contrast can generate different wave fields and hence multiple eigenstates even for a small spherical scatterer. The study was generalized to extended scatterers in [2] and also to electro magnetic waves in [3, 4]. In [26], the number of significant singular values for a finite aperture array is analyzed and in [27] the leading singular values and corresponding singular vectors of the response matrix are further characterized in terms of the location and the dimensions of the extended scatterers in a particular regime.

We can classify a scatterer into three regimes in terms of the size r of the support of the point spread function, i.e., the resolution of the transducer array defined in (2.3). If the size of the scatterer s is much smaller than the resolution r of the array then the scatterer can be regarded as a point scatterer. The response matrix for point scatterers contains only their location information. If s is not much smaller than r then the response matrix contains both the location and size information about the

scatterer as studied in for instance [27]. If s is larger than r, then the rank of the response matrix depends on the ratio s/r [26] and there are many significant singular vectors in the SVD of the response matrix. However, one important point is that each singular vector does not have a clear physical interpretation. In particular each singular vector does not correspond to the illumination vector of a point on the target. Therefore, a particular singular vector does not focus on a point on the target when it is 'time reversed' and sent back. In other words, an extended target can not be interpreted as a collection of point targets. We will show in the next two sections that the response matrix does contain shape (geometry) information of the target up to the resolution of the array, moreover, that if we choose the proper signal space according to the resolution of the array we can image the shape of extended targets.

Figure 2.2(a), (b) and (c) show typical spectra of the singular values in log scale for scatterers of different sizes as classified above. The wavelength is 48h and the target sizes are 1h,5h,35h respectively, where h is the grid size, and the background medium is homogeneous. We use 40 transducers located about 200h from the target and on all four sides.
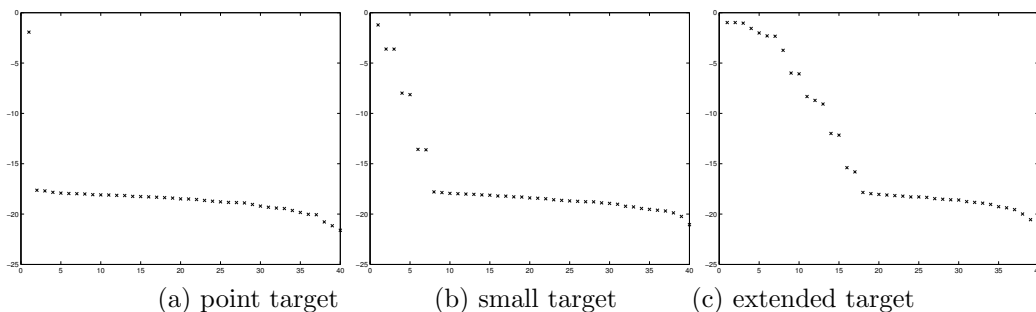

(a) point target   (b) small target   (c) extended target

FIG. 2.2. *The spectrum(log scale) of the response matrix*

3. Imaging Algorithm For Extended Target. From the matched filter point of view, imaging using either time reversal or MUSIC will result in focusings at the sources for the scattered field. In this section we will study the scattered field and the structure of the response matrix for extended targets. In particular we will address the following two crucial issues for imaging extended targets using the MUSIC algorithm (2.6):

- How should one choose properly the set of singular vectors that span the signal space?
- How should one choose the physically correct illumination vector?

Our starting point is based on the boundary integral equation formulation for the scattered field which provides a good understanding of the response matrix and the information it contains.

3.1. Dirichlet Boundary Condition. First, let us assume a Dirichlet boundary condition for the target, i.e., a sound soft target. Let Ω denote the target and Ω^c the exterior of the target. The scattered field u^s satisfies the following equation

$$\begin{cases} \Delta u^s(\boldsymbol{x}) + k^2 u^s(\boldsymbol{x}) = 0 & \boldsymbol{x} \in \Omega^c \subset R^d \\ u^s(\boldsymbol{x}) = -u^i(\boldsymbol{x}) & \boldsymbol{x} \in \partial\Omega \end{cases} \tag{3.1}$$

and in addition a far field radiation condition $r^{\frac{m-1}{2}}(\frac{\partial u}{\partial r} - iku) \to 0$ as $r = |\boldsymbol{x}| \to \infty$. Here u^i is the incident field and m is the space dimension. Let $G_D(\boldsymbol{x}, \boldsymbol{y})$ be the Greens

7

function that satisfies

$$\begin{cases} \Delta G_D(\boldsymbol{x}) + k^2 G_D(\boldsymbol{x}) = \delta(\boldsymbol{x} - \boldsymbol{y}) & \boldsymbol{x}, \boldsymbol{y} \in \Omega^c \subset R^d \\ G_D(\boldsymbol{x}, \boldsymbol{y}) = 0 & \boldsymbol{x} \in \partial\Omega \end{cases} \qquad (3.2)$$

and the same far field radiation boundary condition as above. From Greens formula we have

$$u^s(\boldsymbol{x}) = -\int_{\partial\Omega} u^s(\boldsymbol{y}) \frac{\partial G_D(\boldsymbol{x}, \boldsymbol{y})}{\partial\nu} d\boldsymbol{y} = \int_{\partial\Omega} u^i(\boldsymbol{y}) \frac{\partial G_D(\boldsymbol{x}, \boldsymbol{y})}{\partial\nu} d\boldsymbol{y} \qquad (3.3)$$

where ν is the outward normal at the boundary. The Greens function $G_D(\boldsymbol{x}, \boldsymbol{y})$ is unknown since it depends on the shape of the unknown target. However, u^i is the illumination wave form we can control. If a point source is fired at transducer $\boldsymbol{x}_i$, $u^i(\boldsymbol{y}) = G_0(\boldsymbol{y}, \boldsymbol{x}_i)$. The scattered wave received at $\boldsymbol{x}_j$ is

$$P_{ij} = \int_{\partial\Omega} G_0(\boldsymbol{y}, \boldsymbol{x}_i) \frac{\partial G_D(\boldsymbol{x}_j, \boldsymbol{y})}{\partial\nu} d\boldsymbol{y} = \int_{\partial\Omega} G_0(\boldsymbol{x}_i, \boldsymbol{y}) \frac{\partial G_D(\boldsymbol{x}_j, \boldsymbol{y})}{\partial\nu} d\boldsymbol{y}, \qquad (3.4)$$

where G_0 is the free space Greens function. A physical interpretation is that the source of the scattered wave field is a weighted superposition of monopoles at the boundary. In particular $P_{ij}(= P_{ji})$ is a superposition of the wave field at $\boldsymbol{x}_i$ corresponding to monopoles located at the boundary. The weights are determined by the normal derivatives of the Greens function which corresponds to a point source at $\boldsymbol{x}_j$, e.g., $\frac{\partial G_D(\boldsymbol{y}, \boldsymbol{x}_j)}{\partial\nu}$. It follows that the part of the boundary that is "well illuminated" gives a strong contribution to the response matrix. The response matrix can be written

$$P = \int_{\partial\Omega} \vec{g}_0(\boldsymbol{y}) \left[\frac{\partial\vec{g}(\boldsymbol{y})}{\partial\nu} \right]^T d\boldsymbol{y} \qquad (3.5)$$

where $\vec{g}_0(\boldsymbol{y})$ is the illumination vector

$$\vec{g}_0(\boldsymbol{y}) = [G_0(\boldsymbol{x}_1, \boldsymbol{y}), \dots, G_0(\boldsymbol{x}_N, \boldsymbol{y})]^T \qquad (3.6)$$

and

$$\frac{\partial\vec{g}(\boldsymbol{y})}{\partial\nu} = \left[\frac{\partial G_D(\boldsymbol{x}_1, \boldsymbol{y})}{\partial\nu}, \dots, \frac{\partial G_D(\boldsymbol{x}_N, \boldsymbol{y})}{\partial\nu} \right]^T \qquad (3.7)$$

Equation (3.5) is a factorization of the response matrix that separates known information (the incoming wave) from unknown information. The range of the response matrix is determined by the span of the illumination vectors $\vec{g}_0(\boldsymbol{y})$ corresponding to the well illuminated part of the boundary. Our imaging function is based on the following two observations:

1. The array picks up a certain degree of independent shape information of extended targets depending on the resolution of the array [26]. This information is embedded in a proper collection of leading singular vectors.
2. The illumination vector corresponding to points on well illuminated part of the boundary should be in or close to the subspace spanned by the above collection of leading singular vectors.

Define the **shape space** (or the signal space): $V^S = span\{\vec{v}_1, \vec{v}_2, \dots, \vec{v}_M\}, M < N$, where $\vec{v}_k$'s are the singular vectors of the the response matrix with corresponding

singular values $\sigma_1 \geq \sigma_2 \geq \ldots \geq \sigma_M \geq \mu > 0$ and define the noise space V^N as the orthogonal complement of the shape or signal space, then our imaging function is the MUSIC (2.6) imaging function. From the above two observations, the MUSIC imaging function peaks at points on the boundary of the target. In Section 4 we will show how to estimate a proper cutoff range for M based on the distribution of singular values and resolution analysis and demonstrate that with a proper choice of M the imaging function will peak at the boundary of the target. We will also show that the thresholding provides a proper regularization when there is noise.

Remark 1: The above analysis only claims that the imaging function will peak on the well illuminated boundary parts. However, it does not preclude the possibility of peaks at other points in the domain. Those points are usually inside the boundary and their corresponding illumination vectors may be close to a linear combination of those of the illuminated boundary. Physically this can by explained by resonance or interference patterns. We do encounter such situations in our numerical test, see Figure 5.3.

Remark 2: The SVD corresponds to a principal component analysis and extracts dominant information. The projection operation to the signal space is used for imaging extended targets because it is the collection of leading singular vectors that contains important shape information, note however that each individual singular vector does not have a clear physical meaning.

Remark 3: Numerically all singular vectors are normalized to unit vector in L_2 norm. The illumination vector is also normalized to a unit vector in the imaging function.

3.2. Neumann Boundary Condition. If we have a sound hard target, i.e. the Neumann boundary condition is satisfied at the boundary of the target, the scattered field is:

$$u^s(\boldsymbol{x}) = -\int_{\partial\Omega} \frac{\partial u^i(\boldsymbol{y})}{\partial \nu} G_N(\boldsymbol{x}, \boldsymbol{y}) d\boldsymbol{y} \tag{3.8}$$

where $G_N(\boldsymbol{x}, \boldsymbol{y})$ is the unknown Greens function with Neumann boundary condition. Again u^i is the illumination wave field which we can choose. If we send out a point source at transducer $\boldsymbol{x}_i$, the scattered wave received at $\boldsymbol{x}_j$ is

$$P_{ij} = -\int_{\partial\Omega} \frac{\partial G_0(\boldsymbol{y}, \boldsymbol{x}_i)}{\partial \nu} G_N(\boldsymbol{x}_j, \boldsymbol{y}) d\boldsymbol{y}.$$

In this case the source of the scattered wave field is a weighted superposition of dipoles at the boundary. In particular $P_{ij}(= P_{ji})$ is a superposition of wave field at $\boldsymbol{x}_i$ corresponding to dipoles located at the boundary. The superposition weight is determined by Greens function $G_N(\boldsymbol{y}, \boldsymbol{x}_j)$ at the boundary corresponding to a point source at $\boldsymbol{x}_j$. The response matrix has the following form

$$P = -\int_{\partial\Omega} \left[\frac{\partial \vec{g}_0(\boldsymbol{y})}{\partial \nu} \right] \vec{g}^T(\boldsymbol{y}) d\boldsymbol{y} \tag{3.9}$$

where

$$\frac{\partial \vec{g}_0(\boldsymbol{y})}{\partial \nu} = [\frac{\partial G_0(\boldsymbol{y}, \boldsymbol{x}_1)}{\partial \nu(\boldsymbol{y})}, \ldots, \frac{\partial G_0(\boldsymbol{y}, \boldsymbol{x}_N)}{\partial \nu(\boldsymbol{y})}]^T \tag{3.10}$$

and

$$\vec{g}(\boldsymbol{y}) = [G_N(\boldsymbol{x}_1, \boldsymbol{y}), \ldots, G_N(\boldsymbol{x}_N, \boldsymbol{y})]^T \tag{3.11}$$

9

Now we have a different factorization of the response matrix. So we design our imaging function differently. Suppose the set of leading singular vectors $\vec{v}_1, \vec{v}_2, \ldots, \vec{v}_M, M < N$ span the shape space. The normal derivative of the illumination vector $\frac{\partial \vec{g}_0(\boldsymbol{y})}{\partial \nu(\boldsymbol{y})}$ at the well illuminated part of the boundary should be in or close to the signal space. In other words, we use $\frac{\partial \vec{g}_0(\boldsymbol{y})}{\partial \nu(\boldsymbol{y})}$ to replace the illumination vector $\vec{g}_0(\boldsymbol{y})$ in the imaging function for Dirichlet boundary condition. Since the normal direction at the boundary is also unknown, we use a set of fixed search directions $\nu_l, l = 1, 2, \ldots, L$ at each point and take the maximum among these directions at each point as the imaging function:

$$I(\boldsymbol{y}) = max_l \frac{1}{\|\frac{\partial \vec{g}_0(\boldsymbol{y})}{\partial \nu_l}\|^2 - \sum_{i=1}^{M} | \frac{\partial \vec{g}_0(\boldsymbol{y})^H}{\partial \nu_l} \vec{v}_i |^2} \tag{3.12}$$

This imaging function gives both shape information and an estimate of the normal directions at the boundary.

Remark 4: If we use the wrong imaging function we still get an estimate of the target boundary but with poor quality. In fact, if we use the wrong imaging function the imaging procedure attempts to approximate dipoles by a combination of monopoles and visa versa. We will show this in our numerical tests and how this phenomenon can be used to estimate the material property of a target.

3.3. Other Cases. Consider the impedance boundary condition $\frac{\partial u}{\partial \nu} + i\mu u = 0$ at the target boundary, we have the following integral equation:

$$u^s(\boldsymbol{x}) = \int_{\partial\Omega}\left[i\mu u^s(\boldsymbol{y}) + \frac{\partial u^s(\boldsymbol{y})}{\partial \nu}\right]G_I(\boldsymbol{x}, \boldsymbol{y})dS(\boldsymbol{y}) = -\int_{\partial\Omega}\left[i\mu u^i(\boldsymbol{y}) + \frac{\partial u^i(\boldsymbol{y})}{\partial \nu}\right]G_I(\boldsymbol{x}, \boldsymbol{y})dS(\boldsymbol{y}),$$
$$\tag{3.13}$$

where $G_I(\boldsymbol{x}, \boldsymbol{y})$ is the Greens function with the same impedance boundary condition. If point sources are used for illumination, we have

$$P_{ij} = -\int_{\partial\Omega}\left[i\mu G_0(\boldsymbol{y}, \boldsymbol{x}_i) + \frac{\partial G_0(\boldsymbol{y}, \boldsymbol{x}_i)}{\partial \nu}\right] G_I(\boldsymbol{x}_j, \boldsymbol{y})dS(\boldsymbol{y}). \tag{3.14}$$

Hence, the scattered field is generated by a linear combination of monopoles and dipoles at the boundary. If we know the material property of the targets, i.e., we know μ then we can use this linear combination of a monopole and a dipole as the illumination vector in our imaging function.

In general μ is unknown and we may use the Dirichlet and/or the Neumann imaging functions. For large positive μ, the problem is Dirichlet-like and the Dirichlet imaging function gives good result. For small positive μ, the problem is Neumann-like and the Neumann imaging function gives good result, see Figure 5.5 for an example. Using both can give some indication of the material property of the targets.

For a penetrable target with a constant contrast, we have the following integral equations for the scattered field from potential theory:

$$u^s(\boldsymbol{x}) = \int_{\partial\Omega} \frac{\partial G_0(\boldsymbol{x}, \boldsymbol{y})}{\partial \nu(\boldsymbol{y})}\psi(\boldsymbol{y}) + G_0(\boldsymbol{x}, \boldsymbol{y})\phi(\boldsymbol{y})dS(\boldsymbol{y}) \tag{3.15}$$

where ϕ and ψ are density functions for single and double layer potentials. The inter-element response is then

$$P_{ij} = \int_{\partial\Omega} \frac{\partial G_0(\boldsymbol{x}_j, \boldsymbol{y})}{\partial \nu(\boldsymbol{y})}\psi(\boldsymbol{x}_i, \boldsymbol{y}) + G_0(\boldsymbol{x}_j, \boldsymbol{y})\phi(\boldsymbol{x}_i, \boldsymbol{y})dS(\boldsymbol{y}) \tag{3.16}$$

with $\psi(\boldsymbol{x}_i, \boldsymbol{y}), \phi(\boldsymbol{x}_i, \boldsymbol{y})$ being the density functions for a point source at $\mathbf{x}_i$. Again the source for the scattered field is a combination of monopoles and dipoles located on the boundary. However the weight of the combination changes along the boundary. If Dirichlet and/or Neumann imaging functions are used they both peak near the boundary. See Figure 5.8 for an imaging example.

For a target with a smooth variation of contrast the Lippmann-Schwinger equation gives

$$u^s(\boldsymbol{x}) = \int_\Omega G_0(\boldsymbol{x}, \boldsymbol{y})\sigma(\boldsymbol{y})u(\boldsymbol{y})d\boldsymbol{y}. \tag{3.17}$$

Here σ is the contrast which is a smooth function with compact support. If a point source is used, then the total field $u = u^i + u^s$ is the Greens function with the target included. The inter-element response is therefore

$$P_{ij} = \int_\Omega \sigma(\boldsymbol{y})G_0(\boldsymbol{x}_i, \boldsymbol{y})G(\boldsymbol{x}_j, \boldsymbol{y})d\boldsymbol{y} \tag{3.18}$$

and the response matrix

$$P = \int_\Omega \sigma(\boldsymbol{y})\vec{g}_0(\boldsymbol{y})\vec{g}^T(\boldsymbol{y})dy. \tag{3.19}$$

The integral is now over the whole region Ω and well illuminated high contrast parts, with $\sigma(\boldsymbol{y})G(\boldsymbol{x}_i, \boldsymbol{y})$ relatively large, can be viewed as the sources for the scattered wave field. Hence, the Dirichlet imaging function will peak on those parts in region Ω, see Figure 5.8.

3.4. Another Formulation Using the Total Field. Another formulation is to represent the scattered field in term of the total field $u(\boldsymbol{x}) = u^i(\boldsymbol{x}) + u^s(\boldsymbol{x})$. The scattered field and the incoming field satisfy the following two relations:

$$u^s(\boldsymbol{x}) = \int_{\partial\Omega} G_0(\boldsymbol{x}, \boldsymbol{y})\frac{\partial u^s(\boldsymbol{y})}{\partial\nu} - u^s(\boldsymbol{y})\frac{\partial G_0(\boldsymbol{x}, \boldsymbol{y})}{\partial\nu}d\boldsymbol{y}, \tag{3.20}$$

$$0 = \int_{\partial\Omega} G_0(\boldsymbol{x}, \boldsymbol{y})\frac{\partial u^i(\boldsymbol{y})}{\partial\nu} - u^i(\boldsymbol{y})\frac{\partial G_0(\boldsymbol{x}, \boldsymbol{y})}{\partial\nu}d\boldsymbol{y}, \tag{3.21}$$

If $u(\boldsymbol{x})$ satisfies Dirichlet boundary condition at $\partial\Omega$ the sum of the above two equations gives

$$u^s(\boldsymbol{x}) = \int_{\partial\Omega} G_0(\boldsymbol{x}, \boldsymbol{y})\frac{\partial u(\boldsymbol{y})}{\partial\nu}d\boldsymbol{y}. \tag{3.22}$$

For a point source at $\boldsymbol{x}_i$ the total field is $u(\boldsymbol{x}) = G_D(\boldsymbol{x}, \boldsymbol{x}_i)$. The scattered field at $\boldsymbol{x}_j$ is

$$P_{ij} = \int_{\partial\Omega} G_0(\boldsymbol{x}_j, \boldsymbol{y})\frac{\partial G_D(\boldsymbol{x}_i, \boldsymbol{y})}{\partial\nu}d\boldsymbol{y}, \tag{3.23}$$

which is equivalent to the previous formulation (3.4) and shows the reciprocity of the scattered field. Physically this also gives a dual interpretation: the scattered field at a receiver can be viewed as the normal derivative of the total field (unknown) at target

11

boundary propagated by the free space Greens function. Similar formulations can be derived for other boundary conditions.

When we have an active array, i.e., the transmitters and receivers are at the same place, the response matrix is square and symmetric and these two formulations are equivalent. However, when the array of transmitters and the array of receivers are different the response matrix may not be square anymore and these two formulations can provide complementary information. For example, suppose there are s transmitters located at $\tilde{\boldsymbol{x}}_1, \ldots, \tilde{\boldsymbol{x}}_s$ and there are r receivers located at $\boldsymbol{x}_1, \ldots, \boldsymbol{x}_r$. The response matrix is then of size $s \times r$. For Dirichlet boundary condition the scattered field at jth receiver due to a point source fired at ith transmitter is

$$P_{ij} = \int_{\partial\Omega} G_0(\boldsymbol{y}, \tilde{\boldsymbol{x}}_i) \frac{\partial G_D(\boldsymbol{x}_j, \boldsymbol{y})}{\partial\nu} d\boldsymbol{y}, \tag{3.24}$$

So the response matrix has the following vector form

$$P = \int_{\partial\Omega} \vec{\tilde{g}}_0(\boldsymbol{y}) \left[\frac{\partial \vec{g}(\boldsymbol{y})}{\partial\nu} \right]^T d\boldsymbol{y} \tag{3.25}$$

where $\vec{\tilde{g}}_0(\boldsymbol{y})$ is the illumination vector with respect to the transmitter array

$$\vec{\tilde{g}}_0(\boldsymbol{y}) = [G_0(\tilde{\boldsymbol{x}}_1, \boldsymbol{y}), \ldots, G_0(\tilde{\boldsymbol{x}}_s, \boldsymbol{y})]^T \tag{3.26}$$

and

$$\frac{\partial \vec{g}(\boldsymbol{y})}{\partial\nu} = \left[\frac{\partial G_D(\boldsymbol{x}_1, \boldsymbol{y})}{\partial\nu}, \ldots, \frac{\partial G_D(\boldsymbol{x}_r, \boldsymbol{y})}{\partial\nu} \right]^T \tag{3.27}$$

Based on this formulation we can choose a proper set of left singular vectors to form the column signal space and use illumination vector $\vec{\tilde{g}}_0(\boldsymbol{y})$ in the imaging function.

On the other hand we can use the total field formulation and have

$$P = \int_{\partial\Omega} \left[\frac{\partial \vec{\tilde{g}}(\boldsymbol{y})}{\partial\nu} \right] \vec{g}_0^T(\boldsymbol{y}) d\boldsymbol{y} \tag{3.28}$$

where $\vec{g}_0(\boldsymbol{y})$ is the illumination vector with respect to the receiver array

$$\vec{g}_0(\boldsymbol{y}) = [G_0(\boldsymbol{x}_1, \boldsymbol{y}), \ldots, G_0(\boldsymbol{x}_r, \boldsymbol{y})]^T \tag{3.29}$$

and

$$\frac{\partial \vec{\tilde{g}}(\boldsymbol{y})}{\partial\nu} = \left[\frac{\partial G_D(\tilde{\boldsymbol{x}}_1, \boldsymbol{y})}{\partial\nu}, \ldots, \frac{\partial G_D(\tilde{\boldsymbol{x}}_s, \boldsymbol{y})}{\partial\nu} \right]^T \tag{3.30}$$

So we can also choose a proper set of right singular vectors to form the row signal space and use illumination vector $\vec{g}_0(\boldsymbol{y})$ in the imaging function. Of course by combining these two formulations we incorporate aperture from both the transmitter and the receiver arrays to some extent. We will show examples in section 5.

3.5. Illumination By Plane Waves. In the above formulations the scattered field is factorized into two parts, one is the incoming illumination field which we can choose and the other one is the scattering of the incoming field due to the unknown targets. Instead of point source we can use other forms of illumination. For instance,

12

one can use plane waves of different directions as incoming fields. As an example, with Dirichlet boundary condition the scattered wave field due to an incoming plane wave is

$$u^s(\boldsymbol{x}) = \int_{\partial\Omega} e^{ik\hat{\boldsymbol{x}}\cdot\boldsymbol{y}} \frac{\partial G_D(\boldsymbol{x},\boldsymbol{y})}{\partial\nu} d\boldsymbol{y}, \quad \|\hat{\boldsymbol{x}}\| = 1, \tag{3.31}$$

where $\hat{\boldsymbol{x}}$ is the incident plane wave direction. If we illuminate the targets from s different directions, $\hat{\boldsymbol{x}}_1, \ldots, \hat{\boldsymbol{x}}_s$, and measure the scattered field at r locations $\boldsymbol{x}_1, \ldots, \boldsymbol{x}_r$ the response matrix will be of size $s \times r$ with elements

$$P_{ij} = \int_{\partial\Omega} e^{ik\hat{\boldsymbol{x}}_i\cdot\boldsymbol{y}} \frac{\partial G_D(\boldsymbol{x}_j,\boldsymbol{y})}{\partial\nu} d\boldsymbol{y}$$

representing the scattered field measured at jth receiver due to a plane wave in the ith direction. Here there is no symmetric relation, e.g. $P_{ij} \neq P_{ji}$. In matrix form we have

$$P = \int_{\partial\Omega} \hat{g}(\boldsymbol{y}) \left[\frac{\partial\vec{g}(\boldsymbol{y})}{\partial\nu} \right]^T d\boldsymbol{y}, \tag{3.32}$$

where

$$\hat{g}(\boldsymbol{y}) = [e^{ik\hat{\boldsymbol{x}}_1\cdot\boldsymbol{y}}, \ldots e^{ik\hat{\boldsymbol{x}}_s\cdot\boldsymbol{y}}]^T.$$

So we can define a column signal space using a proper set of leading left singular vectors and use $\hat{g}(\boldsymbol{y})$ as the illumination vector in the imaging function.

We can also use the total field formulation and have

$$u^s(\boldsymbol{x}) = \int_{\partial\Omega} G_0(\boldsymbol{x},\boldsymbol{y}) \frac{\partial u(\boldsymbol{y})}{\partial\nu} d\boldsymbol{y}, \tag{3.33}$$

where u is the total field due to an incident plane wave. Let u_i denote the total wave field due to the ith incoming plane wave. We have

$$P_{ij} = \int_{\partial\Omega} G_0(\boldsymbol{x}_j,\boldsymbol{y}) \frac{\partial u_i(\boldsymbol{y})}{\partial\nu} d\boldsymbol{y},$$

These two equivalent formulations correspond to the duality and mixed reciprocity between plane waves and point sources [18] in the sense that the scattered field at a point $\boldsymbol{y}$ due to an incident plane wave with direction $-\hat{\boldsymbol{x}}$ is proportional to the far field at the direction $\hat{\boldsymbol{x}}$ due to a point source located at $\boldsymbol{y}$. The response matrix takes the following form

$$P = \int_{\partial\Omega} \left[\frac{\partial\vec{u}(\boldsymbol{y})}{\partial\nu} \right] \vec{g}_0^T(\boldsymbol{y}) d\boldsymbol{y}, \tag{3.34}$$

where $\vec{u} = [u_1, \ldots, u_s]^T$ and $\vec{g}_0$ is the illumination vector defined by the free space Greens function in (3.6). In other words, we can use leading right singular vectors to define a row signal space and use $\vec{g}_0$ as the illumination vector in the imaging function, or we can combine both of these two formulations.

13

3.6. Dealing With Noise And Inhomogeneity. In real applications noise, such as measurement noise, is always present. Moreover, the background medium may contain some inhomogeneity, i.e., we do not know the exact form of the background Greens function. We can model the measured field at the array in the form

$$P_{ij} = \int_{\partial\Omega} \frac{\partial G_T(\boldsymbol{x}_j, \boldsymbol{y})}{\partial\nu} G_B(\boldsymbol{x}_i, \boldsymbol{y}) d\boldsymbol{y} \ (+ \text{ or } \times) \text{ measurement noise} \qquad (3.35)$$

assuming a Dirichlet boundary condition. This formulation separates the target information, embedded in Greens function G_T, from the background medium information, embedded in G_B. If the signal to noise ratio (SNR) in the measurement is high in the sense that the signal from scattering at the targets is stronger than the scattering of background inhomogeneities and the measurement noise, the SVD can still extract dominant information or the principal components from the measurement as is demonstrated in our tests in Section 5. Since scattering at the targets is coherent for different frequencies, using multiple frequencies and averaging will increase the signal to noise ratio and the robustness of the imaging procedure.

Remark 5: In general the strength of the background inhomogeneity depends on the medium variation, both the contrast and the scale of the variation, and the propagation distance from the array to the target. Any knowledge that improves the approximation of the background Greens function will result in better imaging. In particular we can (1) incorporate multiple scattering of the background medium, such as reflections of walls, into the background Greens function, (2) derive effective medium property to ignore small scale variations in the background medium.

4. Resolution And Noise Level Based Thresholding. Here we carry out a resolution analysis to characterize the signal space and give a guideline for choosing a proper set of significant singular vectors that contains the shape information and spans the signal space V^S. The orthogonal complement is defined as the noise space V^N as in (2.6). We consider only sound-soft target(s) in this study.

First, we develop a resolution based thresholding strategy. Let M be the number of leading singular vectors that span the signal space. In the case of uniform illumination of the boundary, our thresholding strategy is based on the following relation

$$\frac{D}{r} = CM, \qquad (4.1)$$

where D is the perimeter (or dimension) of the target(s) boundary, r is the corresponding scale of the resolution for the array and C is a dimensionless factor of proportionality. In more general situations the above relation will be more complicated. For example, the material properties of the target, such as contrast, may affect the constant C. Moreover, the geometry of the boundary, such as concavity, and the configuration of the array, such as limited aperture, will affect the illumination strength at different parts of the boundary. When the target is not in the near field the resolution of the array is proportional to $\lambda L/a$, where λ is the wavelength, L is the distance from the array to the target and a is the aperture of the array. Thus we have the following relation [26]:

$$\frac{Da}{\lambda L} = CM \quad \Rightarrow \quad M \propto \frac{1}{\lambda}, \qquad (4.2)$$

e.g., the dimension of the signal space should be inversely proportional to the wavelength. In many applications L and a are fixed. We vary λ and use this proportionality relation to determine the thresholding.

14

shape	λ	L	a	δ	D	predict	invariance estimate
circle	λ_0	L_0	a_0	δ_0	D_0		12
circle	λ_0	L_0	a_0	δ_0	$2D_0$	24	24
circle	$\frac{3}{2}\lambda_0$	L_0	a_0	δ_0	$2D_0$	16	16
circle	λ_0	L_0	a_0	$2\delta_0$	D_0	12	12
circle	λ_0	L_0	$\frac{5}{8}a_0$	δ_0	D_0	7.5	8
circle	λ_0	$\frac{2}{3}L_0$	$\frac{2}{3}a_0$	$\frac{2}{3}\delta_0$	$\frac{4}{3}D_0$	16	16
ellipse	λ_0	L_0	a_0	δ_0	$\frac{4.967}{\pi}D_0$	18.97	18
rectangle	λ_0	L_0	a_0	δ_0	$\frac{6}{\pi}D_0$	22.92	24
triangle	λ_0	L_0	a_0	δ_0	$\frac{4+2\sqrt{2}}{\pi}D_0$	26.08	23
7 leaves	λ_0	L_0	a_0	δ_0	$\frac{7.767}{2\pi}D_0$	14.83	14
2 circles	λ_0	$\approx L_0$	a_0	δ_0	$2D_0$	24	22

TABLE 4.1

Numerical justification of the invariance of the signal-to-noise ratio. Notice that the last two columns of the table almost agree.

Next, we define a signal to noise ratio that will be helpful in order to estimate the number of singular vectors M. Let $P = U\Sigma V^H$ be the singular value decomposition of the response matrix and $\sigma_1 \geq \sigma_2 \geq \ldots \geq \sigma_M$ be the singular values of the response matrix that span the signal space V^S. Define the signal-to-noise ratio:

$$\frac{\|P_{signal}\|_2}{\|P_{noise}\|_2} = \frac{\sigma_1}{\sigma_{M+1}} \, ,$$

where $P_{signal} = U_M \Sigma_M V_M^H$ with U_M, V_M denoting the first M columns of U and V, respectively, Σ_M being the corresponding submatrix of Σ and $P_{noise} = P - P_{signal}$. With correct M, this ratio represents the relative received energy of the scattered wave due to the target(s) versus the energy scattered by the background medium and/or noise. We claim that σ_1/σ_{M+1} is a robust and stable quantity that is invariant to the wavelength. It is a quantity that is stable with respect to the structure of the experiment. We performed extensive numerical simulations which show that this quantity depends only weakly on the parameters:

1. λ: wavelength
2. L: average distance from the transducers to the target(s)
3. a: aperture of the transducer array
4. δ: spacing between two adjacent transducers
5. D: perimeter of the target(s) boundary that is well illuminated.

We illustrate this with a numerical test. In this experiment we use a circular array with evenly spaced transducers in a homogeneous medium. We change the parameters listed above as well as the geometry and size of the targets. Let M_0 be the dimension of the signal space when the parameters $(\lambda_0, L_0, a_0, \delta_0, D_0)$ are used. Pick a threshold ϵ such that $\sigma_1/\sigma_M < \epsilon \leq \sigma_1/\sigma_{M+1}$. This experiment is set as the reference case. For any other parameter sets, we first use the relation $Da/\lambda L = CM$ to get the '**predicted**' value of M and then use the same ϵ to find the '**invariance estimate**' of M, that is a value of M such that $\sigma_1/\sigma_M < \epsilon \leq \sigma_1/\sigma_{M+1}$. The results are given in table 4.1 and we see that the invariance estimate is close to the predicted value of M.

Here we propose to use the invariance of the signal to noise ratio at different

frequencies to estimate M and describe this procedure next. Let σ_i^j be the i'th singular value for the response matrix that corresponds to the j'th frequency for $j \in \{1, \cdots, m\}$. Let

$$R_j(M_j) = \sigma_1^j / \sigma_{M_{j+1}}^j$$

be the signal to noise ratio for the j'th frequency or wavelength, where M_j is the number of singular vectors that span the signal space. According to the resolution analysis, $\lambda_j M_j$ is close to a constant, where λ_j is the j'th wavelength. We have therefore $M_j \approx (\lambda_m / \lambda_j) M_m$. We now construct the following function of $\hat{M}_m$:

$$f(\hat{M}_m) = \frac{1}{m-1} \sum_{j=2}^{m} \frac{\mid R_j(\hat{M}_j) - R_1(\hat{M}_1) \mid}{R_1(\hat{M}_1)} , \tag{4.3}$$

where we **define** $\hat{M}_j = (\lambda_m / \lambda_j) \hat{M}_m$. If the 'correct' $\hat{M}_m$ is chosen, that is, $\hat{M}_m \approx M_m$, then $f(\hat{M}_m)$ is **close to zero**. If we plot $f(\hat{M})$ as a function of $\hat{M}$, the pattern is quite clear and with many frequencies we shall demonstrate that the pattern is quite clear even with noise. In particular we would like to make the following remarks:

1. There is an **invariance principle** for the signal to noise ratio that gives: $f(\hat{M}_m) \approx 0$ for $\hat{M}_m = M_m$.
2. For $\hat{M}_m > M_m$, since the signal-to-noise ratio is large $f(\hat{M}_m)$ will in general be large. For $\hat{M}_m < M_m$, if the first few singular values are close to each other, which may happen for large extended targets, then the average of relative errors $f(\hat{M}_m)$ could be close to zero. Thus we estimate M_m as the largest value of $\hat{M}_m$ so that $f(\hat{M}_m)$ is small and has a significant increment afterwards. This pattern can be easily identified from the plot of f versus $\hat{M}_m$. See Figure 5.1.
3. In general it is better to have the lowest frequency (the longest wave length) as the reference, e.g., the mth frequency in (4.3) because (1) the low frequency is more robust; (2) its signal space has the smallest dimension.
4. Usually the number of significant singular vectors M can vary in a range which all give a good approximation of the signal space and good imaging results. The range is of a certain percentage of the total information, i.e., the rank of the
5. When the noise level or heterogeneities in the medium increased, the tail of the spectrum corresponding to the SVD of the response matrix decays relatively slowly. Thus, it will also make the pattern of the $f(\hat{M}_m)$ less clear. However, if we can estimate the correct dimension M of the signal space from prior or other information, our imaging algorithm will be quite robust with respect to noise.

In Section 5 we present numerical examples that illustrate the above points and show that invariance based estimate of M gives good results in general, in particular also in the case with measurement noise.

5. Numerical Experiments. We present numerical experiments that demonstrate the thresholding algorithm for determining the signal space, imaging of extended targets for different boundary conditions and penetrable objects and the robustness of this procedure. In all the examples below the calculation domain is $499h$-by-$499h$, where h is the grid size, and we use a Helmholtz solver with PML [1] for the forward problem in order to generate the response matrix. The search box for the

16

imaging is chosen to be (191:310,191:310) for most experiments and for the imaging figures we use a coordinate system with the origin at (191,191).

5.1. Thresholding. We first illustrate the performance of the thresholding algorithm. We use the kite shape as in [16] and a Dirichlet boundary condition: $u = 0$ on the boundary of the kite. There are 80 transducers that can send and receive signals and that are evenly placed on a circle of radius $200h$ centered at (250,250) in the calculation domain mentioned above. In the examples we show the MUSIC imaging function $I(x) = 1/(\|\vec{g}^0(x)\|^2 - \sum_{k=1}^{M} |\vec{g}^0(x) \cdot \vec{u_k}|^2)$, where M is the number of singular vectors that span the signal space. The thresholding is determined by the choice of M and in order to calculate this threshold we use the wavelengths: $\lambda_1, \cdots, \lambda_5 = 16h, 24h, 32h, 48h, 96h$. We determine M by the invariance estimate introduced in Section 4:

- σ_i^j is the i'th singular value for the response matrix at the j'th wavelength.
- Let $R_j = \sigma_1^j/\sigma_{\hat{M}_{j+1}}^j$ and $\hat{M}_j = \hat{M}_m(\lambda_j/\lambda_m)$.
- As discussed in Section 4, we plot the average of the relative errors

$$f(\hat{M}_m) = \frac{1}{m-1} \sum_{j=2}^{m} \frac{|R_j - R_1|}{R_1}$$

as function of $\hat{M}_m$ in Figure 5.1, with here $m = 5$. We consider both clean data and data with 10% multiplicative noise. From both pictures we see that the relative error is small for $\hat{M}_m = 4$ but increase significantly afterwards. So we take $M_5 = 4$ as the dimension of the signal space for $\lambda = 96h$ and scale it accordingly for other wavelengths.

Figure 5.2 shows the imaging function using the shortest wavelength, $\lambda_1 = 16h$, and $\hat{M}_1$=1,5,18,24,30,36,42 and 48. Note that $\lambda_5 = 96h$ so $\hat{M}_1 = 6\hat{M}_5 = 24$ is the number we should use in imaging according to our resolution analysis and noise level based thresholding. Observe that the imaging result is good for $\hat{M}_1$ in the range from 18 to 36, which illustrates that the imaging has some robustness with respect to the choice of $\hat{M}_1$. It also seems that the very first few singular vectors contain information of strong scattering parts of the target such as sharp features like tips or corners. Moreover the results clearly show that (1) each singular vector does not correspond to a point on the target; (2) the shape information is embedded collectively in a subset of singular vectors.

5.2. Imaging For Different Boundary Conditions. We next present imaging results with our algorithm for extended targets with different boundary conditions which correspond to different material properties of the targets. Our method is also capable of imaging penetrable extended targets with smooth transition of contrast or a constant jump of contrast, as we discussed in Section 3. We use the noise level based thresholding introduced in the previous section to determine how many singular vectors to use in each experiment. There are 80 transducers with equal spacing that surround the target(s), the radius of the transducer array is $200h$ and the wave length is $16h$.

Figure 5.3 shows the imaging function for sound-soft or Dirichlet boundary condition in homogeneous medium. Figure 5.3(a) shows a target with the shape of 5 leaves, $40(1+0.2\cos(5\theta))h$. We observe large values of the imaging function on the boundary of the target. There are also some spots inside the targets with large values, as predicted in Remark 1 in Section 3. Figure 5.3(b) shows the result for several extended
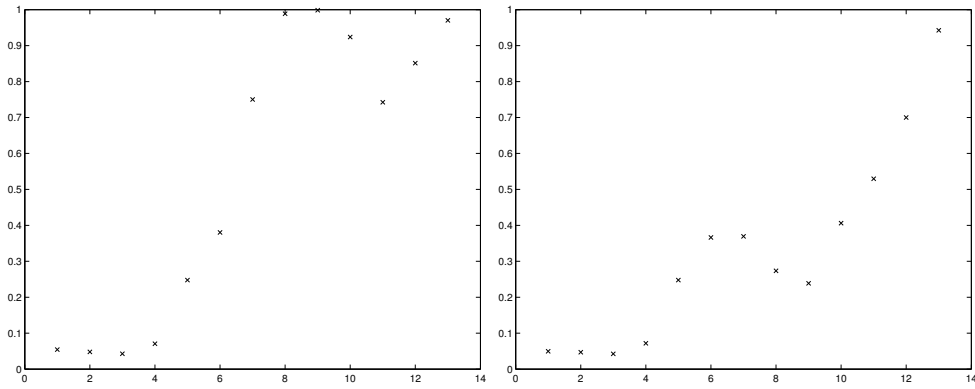
FIG. 5.1. *These pictures are the plot of the function $f(\hat{M})$ for the thresholding criteria, the horizontal axis is the number of singular vectors used for $\lambda = 96h$, the vertical axis is the average of the relative errors. Left: clean data; Right: 10% mulitplicative noise. Both figures indicate that the first big increment is from the 4th to the 5th value of f.*
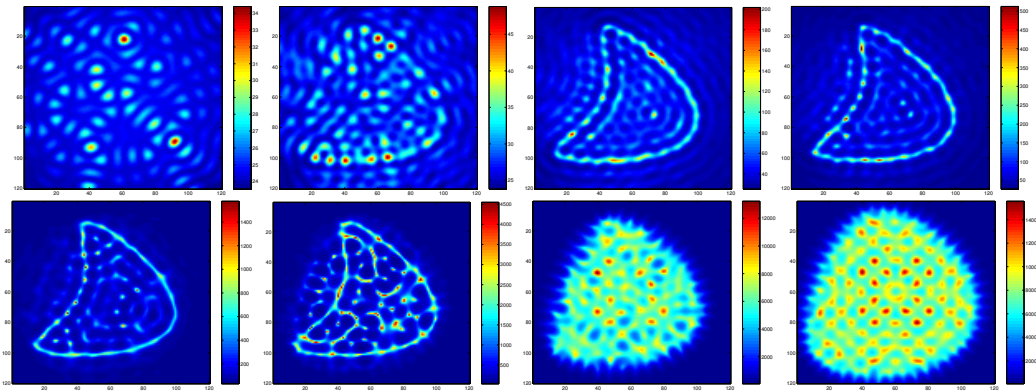

FIG. 5.2. *A slide show of using different number of leading singular vectors (first row: 1,5,18,24; second row: 30,36,42,48) to define the signal space for imaging when we use 80 transducers.*

objects without changing the imaging function. We obtain good imaging results as long as the targets are well separated or the multiple scattering is not strong.

Consider now the case with a Neumann boundary condition for the target. Figure 5.4(a) shows the Neumann imaging function (3.12) using 25 fixed equally distributed search directions for the normal derivative and we see that the boundary is clearly resolved. If instead we use the Dirichlet imaging function, the image will be blurred. See Figure 5.4(b). In fact, the imaging function then gives two boundary curves corresponding to a dipole approximation using a combination of two monopoles. (In all the figures, with boundary curves, we use the darkest color to draw the true solution.) Vice versa, if we use the Neumann imaging function for a sound-soft target, two boundary curves will also result.

Figure 5.5(a) and (b) show imaging results using Dirichlet and Neumann imaging functions for impedance boundary condition with $\mu = 0.2$(small μ, Neumann-like). Figure 5.6 (a) and (b) show the Dirichlet and Neumann imaging function for impedance boundary condition with $\mu = 2$(big μ, Dirichlet-like). This shows that if we use both imaging functions on an unknown target we can get an estimate of the

18
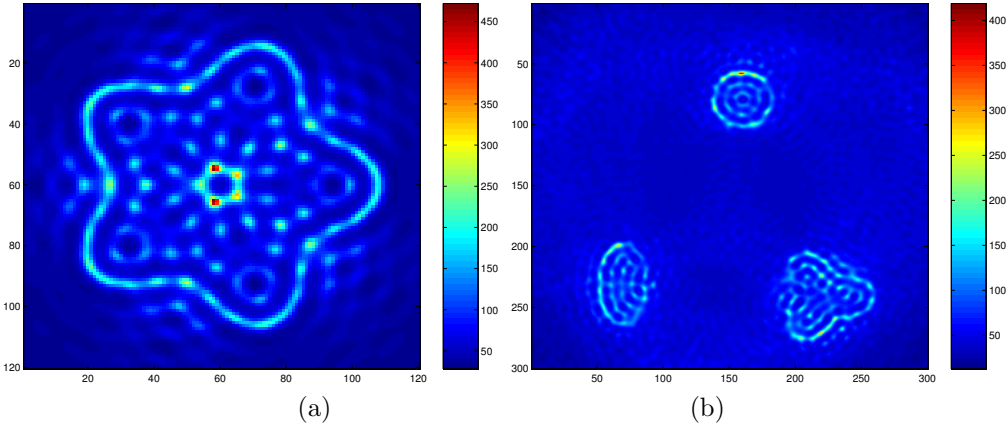
FIG. 5.3. *Imaging of a single (left) and multiple (right) sound-soft target(s) in homogeneous medium.*

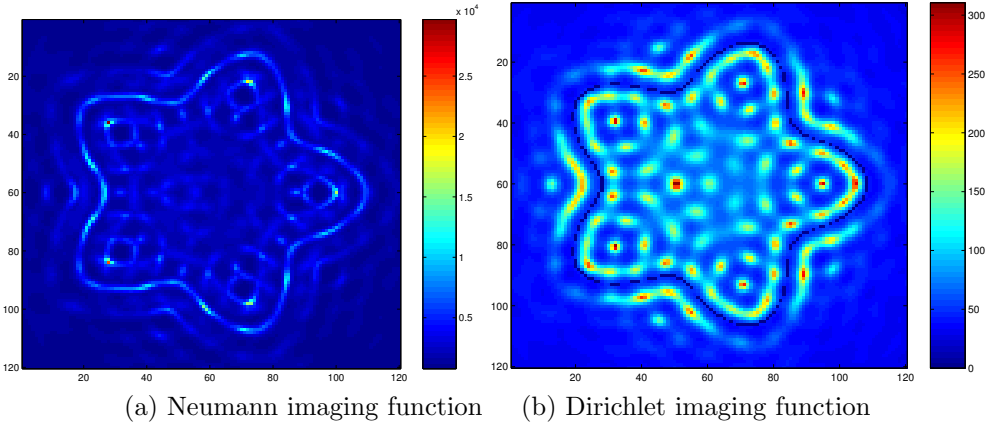(a) Neumann imaging function   (b) Dirichlet imaging function

FIG. 5.4. *Imaging of a sound-hard target.*

shape as well as the material property of the target.

Figure 5.7(a) and (b) show the Dirichlet and Neumann imaging functions for a **mixed boundary condition** (partially coated target). On the upper half of the boundary, the parameter in the Robin condition is $\mu = 0.2$(Neumann-like) and on the lower half $\mu = 2$(Dirichlet-like). We find that the Dirichlet imaging function gives good result for the Dirichlet-like part of the boundary and gives two boundaries for the Neumann-like part of the boundary and vice versa. If the object is partially coated by dielectric our method can therefore be used to detect the coating.

Figure 5.8(a) shows the Dirichlet imaging function for a circular shape target with smooth transition of contrast, that is, the contrast is a smooth function on the boundary of the target. As predicted by the Lippmann-Schwinger equation in Section 3, the imaging function peaks inside the target. Figure 5.8(b) shows the Dirichlet imaging function for a circular shape target with constant contrast. As predicted by potential theory in Section 3, the imaging function peaks near the boundary of the target.

(a) Dirichlet imaging function   (b) Neumann imaging function
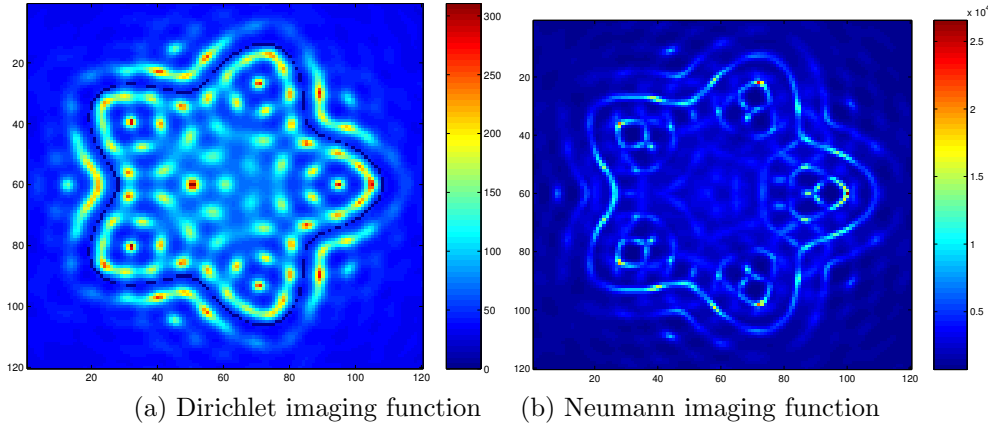
FIG. 5.5. *Imaging of a target with Robin boundary condition with $\mu = 0.2$(Neumann-like).*

(a) Dirichlet imaging function   (b) Neumann imaging function
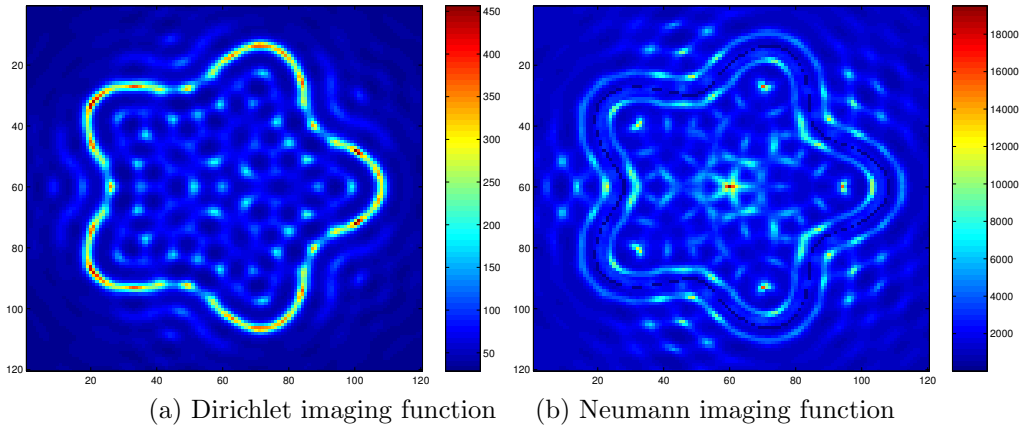
FIG. 5.6. *Imaging of a target with Robin boundary condition with $\mu = 2$(Dirichlet-like)*

5.3. Imaging With Different Transmitter And Receiver Array. Consider first the case when there are 80 transducers surrounding the target. There are 40 transmitters and 40 receivers and they are arranged alternatingly, i.e., using 40 odd label of transducers as transmitters and 40 even label of transducers as receivers. Figure 5.9 (a) and (b) show the imaging results using left (right) singular vectors with illumination vectors to the transmitter (receiver) array respectively. Since both of the transmitter array and the receiver array have the same full aperture, the results are comparable.

Figure 5.10 shows the imaging results using 40 lower transducers as transmitters and 40 upper transducers as receivers. So the aperture is limited for both transmitter and receiver arrays. To get good result we combine the two imaging functions for transmitter and receiver arrays and the figure shows the sum.

5.4. Imaging Using Incident Plane Waves. Now we give some examples with **incident plane waves** instead of point sources. The parameters are chosen as above and we use the same criterion for thresholding as in the point source case. The imaging function uses the corresponding plane wave illumination vectors as described in Section 3.5. There are 80 directions of plane waves and 80 receivers on a circle, i.e.,
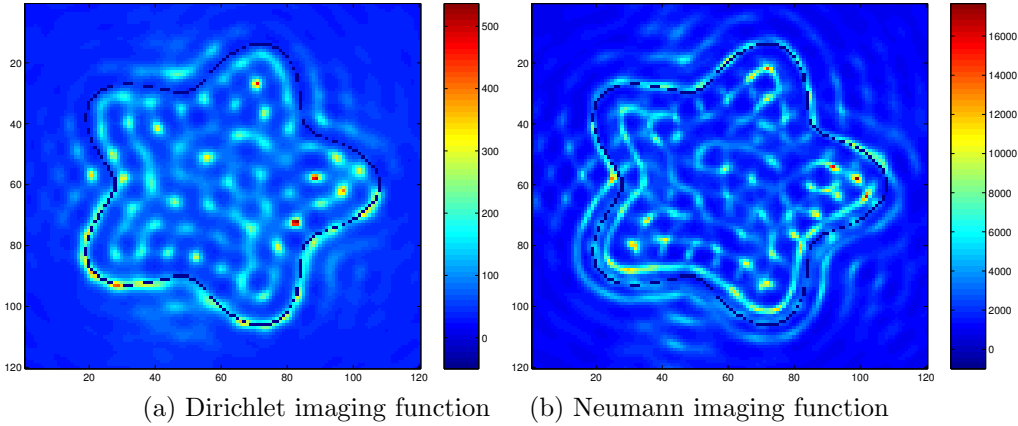
(a) Dirichlet imaging function   (b) Neumann imaging function

FIG. 5.7.   *Imaging of a target with mixed boundary condition, on the upper half $\mu = 0.2$(Neumann-like) and on the lower half $\mu = 2$(Dirichlet-like); darkest color corresponds to the true solution*
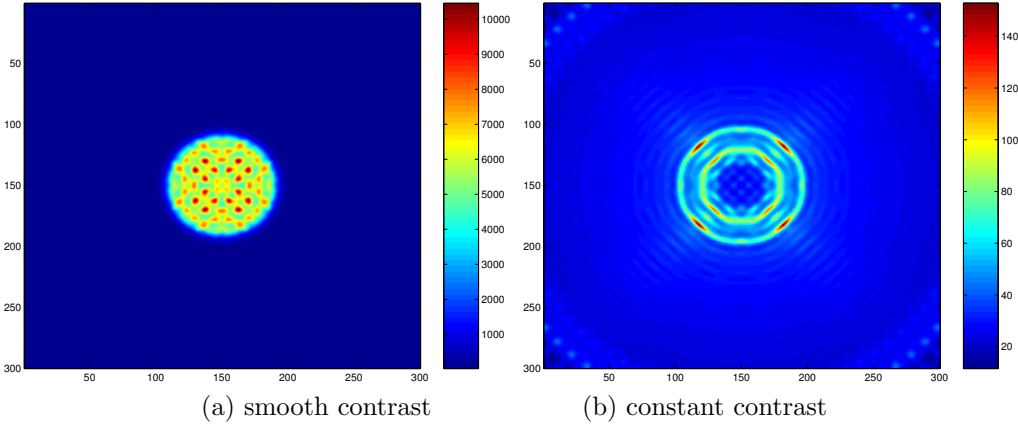

(a) smooth contrast   (b) constant contrast

FIG. 5.8.   *Imaging of a circular shape target with smooth transition of contrast (left) and constant contrast (right)*

the response matrix has dimension 80x80. In this test, the directions and transducers are distributed evenly on the circle. Figure 5.11(a) shows the result for a 5-leaf shape with Dirichlet boundary condition and Figure 5.11(b) shows the result for a 5-leaf penetrable object with a constant contrast, (the wave length inside equals $\sqrt{2}/2$ times the wave length outside the object). We see that in both cases our imaging algorithm identifies the shape of the object.

5.5. Imaging Robustness. Next we illustrate the robustness of the thresholding strategy with respect to multiplicative noise and also random medium fluctuations. Here we use the same number of singular vectors as in the clean case. Of course, in practice, getting a good estimate of the number singular vectors can be challenging when the noise level is high.

First, we consider the robustness with respect to **multiplicative noise**. Figure 5.12 shows the result for the kite shape with noise free data, 100% multiplicative noise and 200% multiplicative noise, respectively. We introduce the noise as follows:
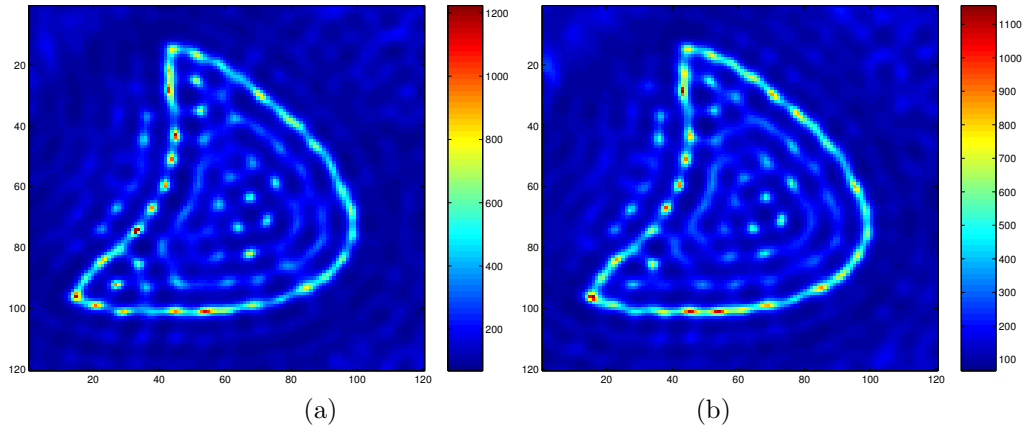
FIG. 5.9. *Imaging of a target. Left: using left singular vectors with illumination vector to the transmitter array; Right: using right singular vectors with illumination vector to the receiver array;*
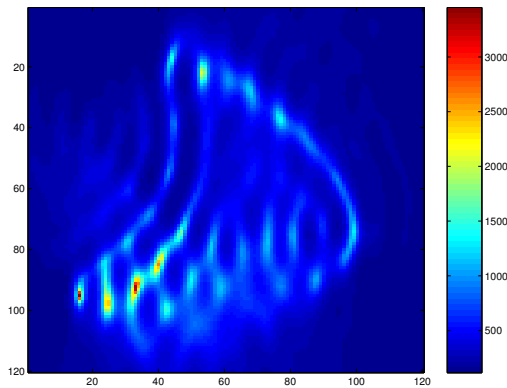

FIG. 5.10. *Imaging of a target with 40 lower transducers as transmitters and 40 upper transducers as receivers. The plot is the sum of two imaging functions*

The real and imaginary part of each entry in the response matrix is multiplied by a factor $1 + \nu$ with ν uniformly distributed and independent for the real and imaginary parts and the different frequencies and matrix entries. There are 40 transducers that surround the target. Figure 5.13 shows the result using 80 instead of 40 transducers. Clearly, using more transducers gives more robust imaging.

Figure 5.14 shows the result for the kite shape in a random medium with 5% standard deviation and correlation length $10h$. The target is well resolved also in this case even though only the homogeneous Greens function is used in the imaging.

Figure 5.15 shows the result for the kite shape with 400% multiplicative noise using two different frequencies. We see that imaging with the lower frequencies, that is a longer wavelength, gives a more robust result.

Our imaging algorithm could also handle 100% standard deviation Gaussian multiplicative noise with very promising result.

In the situation with multiplicative measurement noise or medium noise that are independent for different frequencies we next enhance the imaging robustness by

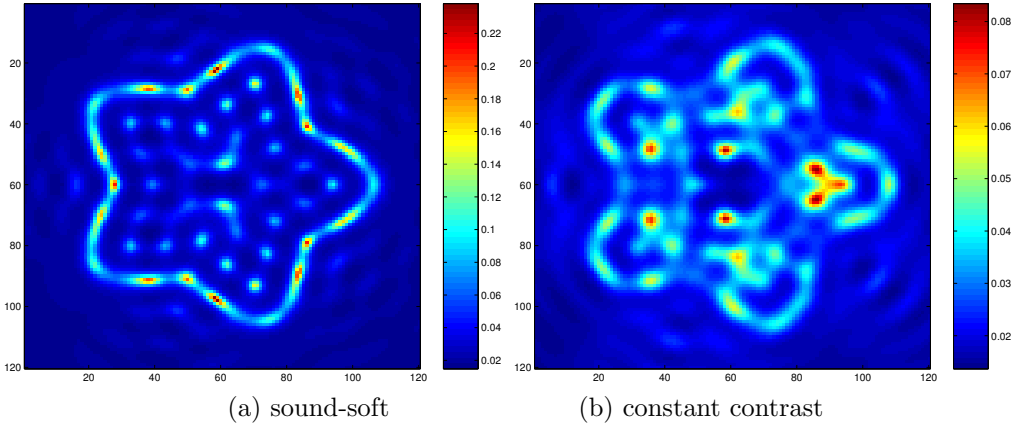(a) sound-soft　　　　　　　(b) constant contrast

FIG. 5.11. *Imaging of an extended target with incident plane waves*

combining several frequencies. The multifrequency imaging function is chosen as:

$$I(\boldsymbol{x}) = \sum_{i=1}^{m} \sum_{k=1}^{M_i} \mid \vec{g}^0(x, \lambda_i) \cdot \vec{u}_k(\lambda_i) \mid^2 / \|\vec{g}^0(x, \lambda_i)\|^2$$

where we explicitly show the frequency dependence. Here m is the total number of frequencies, M_i denotes the number of significant singular vectors for ith frequency and λ_i is the wavelength for ith frequency. Note that the summation over the frequencies stabilize statistically the projection to the signal space.
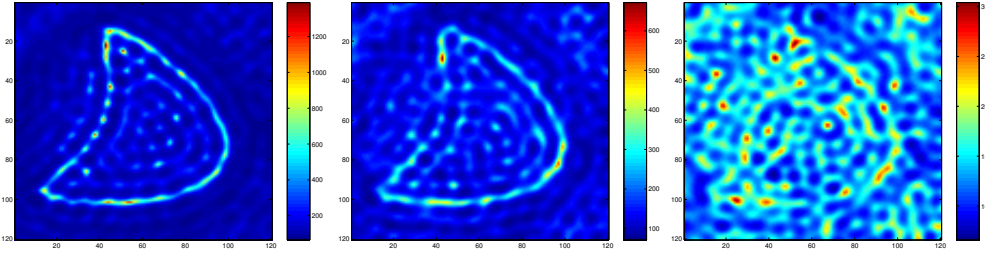
FIG. 5.12. *Imaging of a target using 40 transducers, left: clean data, middle: 100% noise, right: 200% noise*
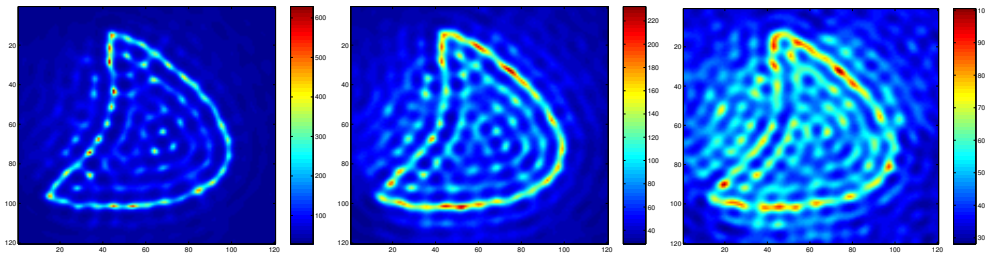
FIG. 5.13. *Imaging of a target using 80 transducers, left: clean data, middle: 100% noise, right: 200% noise*
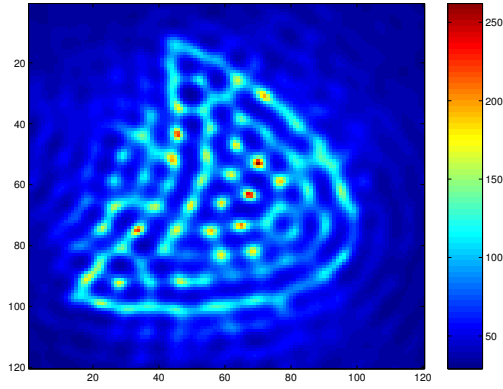
23

FIG. 5.14. *Imaging of a target using 80 transducers, $\lambda = 16h$ in 5% Gaussian random medium with correlation length $10h$*
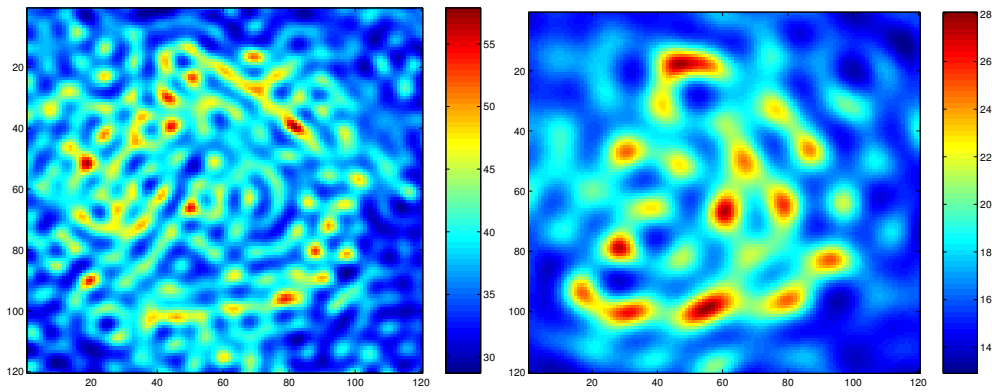

FIG. 5.15. *Imaging of a target using 80 transducers, 400% noise, left: $\lambda = 16h$(high frequency), right: $\lambda = 32h$(low frequency)*

Figure 5.16 shows the result for the kite shape with 200% multiplicative noise in the data. 80 transducers are used. The left figure shows the result using a single frequency($\lambda = 16h$) and the right figure is the result using 3 frequencies($\lambda = 16h, 24h, 32h$). According to the noise level and resolution analysis based thresholding, the number of singular vectors used are chosen to be 25, 17, 13 respectively. Clearly the result for multiple frequencies is much better than that of a single frequency.

Finally, we show how multifrequency information can be used to obtain robust imaging results also in the case with **random fluctuations in the background medium**. The information at different frequencies decorrelate rapidly with the frequency separation [11], therefore, using several frequencies stabilize the imaging result with respect to medium noise.

Figure 5.17 shows the result for the kite shape in a random medium with 10% standard deviation and correlation length $10h$ when 80 transducers are used. The left figure shows the result using a single frequency($\lambda = 16h$). The right figure is the result using 3 frequencies($\lambda = 16h, 24h, 32h$). According to the noise level and resolution analysis based thresholding, the number of singular vectors used are chosen
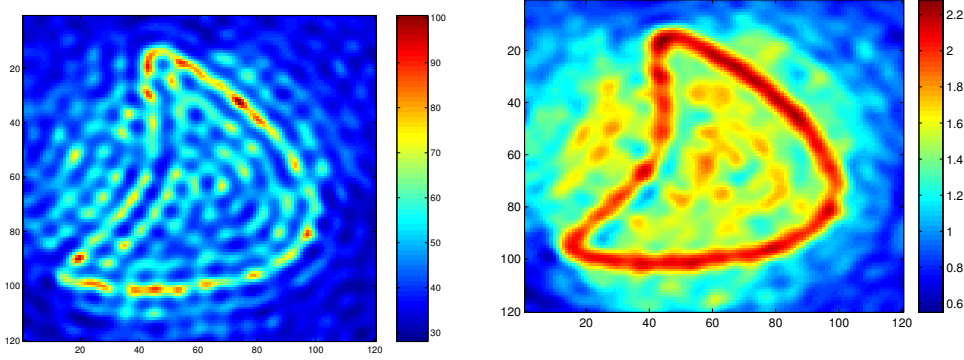
24

FIG. 5.16. *Imaging of a target using 80 transducers, 200% noise, left: $\lambda = 16h$, right: combining $\lambda = 16h, 24h, 32h$*

to be 25, 17, 13 respectively. Again the result for multiple frequencies is much better than that of a single frequency.
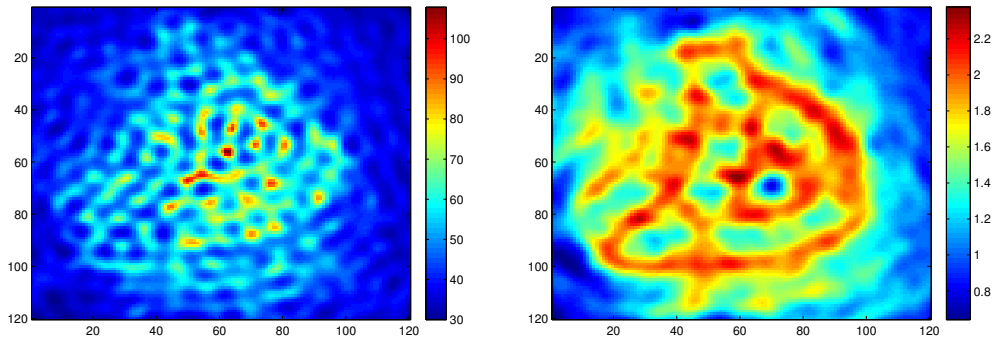

FIG. 5.17. *Imaging of a target using 80 transducers, 10% random medium, left: $\lambda = 16h$, right: combining $\lambda = 16h, 24h, 32h$*

6. Conclusions. We propose a direct imaging algorithm for extended targets. The algorithm is simple and efficient because no forward solver or iteration is needed. The algorithm can also deal with different material properties and different type of illuminations and measurements. The starting point is to locate and visualize strong scattering events that generate the scattered field. A key point in this study is to understand the structure of the measurements based on a physical factorization of the response matrix. Singular value decomposition (SVD) of the response matrix is used to extract information for the dominant scattering events. A crucial and challenging step is the choice of thresholding and regularization, that is, the number of leading singular vectors to be used to define the signal space in the imaging algorithm. A physical resolution based thresholding strategy using multiple frequencies is developed. By an appropriate choice of illumination vectors, different material properties and incoming wave fields can be handled by the imaging algorithm. The proposed imaging algorithm is robust with respect to measurement noise, this derives

25

from the fact that the singular vectors are stable with respect to such noise for large transducer arrays. The imaging procedure is also robust and stable with respect to small medium fluctuations when we use multiple frequencies. This follows due to rapid decorrelation of the response matrix at different frequencies, that is, a narrow coherence bandwidth in the case with long propagation lengths, the situation when the medium noise becomes important. In future work we will look at the effects of limited aperture.

REFERENCES

[1] J.-P. Berenger. A perfectly matched layer for the absorption of electromagnetic waves. *J. Computational Physics*, 1994.

[2] D. H. Chambers. Analysis of the time-reversal operator for scatterers of finite size. *Journal of the Acoustical Society of America*, 112(2):411–419, 2002.

[3] D. H. Chambers and J. G. Berryman. Analysis of the time-reversal operator for a small spherical scatterer in an electromagnetic field. *IEEE Trans. Ant. Prop.*, 2004.

[4] D. H. Chambers and J. G. Berryman. Time-reversal analysis for scatterer characterization. *Phys. Rev. Letters*, 2004.

[5] D. H. Chambers, J. V. Candy, S. K. Lehman, J. S. Kallman, A. J. Poggio, and A. W. Meyer. Time reversal and the spatio-temporal matched filter (l). *J. Acoust. Soc. Am.*, 2004.

[6] D.H. Chambers and A.K. Gautesen. Time reversal for a single spherical scatter. *Journal of the Acoustical Society of America*, 109(6):2616–2614, 2001.

[7] M. Cheney. The linear sampling method and the music algorithm, 2001.

[8] D. Colton and A. Kirsch. A simple method for solving inverse scattering problems in the resonance region. *Inverse Problems*, 1996.

[9] Devaney. Super-resolution processing of multi-static data using time-reversal and MUSIC. *to appear in Journal of the Acoustical Society of America*.

[10] A. J. Devaney F. K. Gruber, E. A. Marengo. Time-reversal imaging with multiple signal classification considering multiple scattering between the targets, 2004.

[11] A. Fannjiang and K. Solna. Time reversal of parabolic waves and two-frequency wigner distribution. *Discrete and Continuous Dynamical Systems*, 2006.

[12] F. K. Gruber, E. A. Marengo, and A. J. Devaney. Time-reversal imaging with multiple signal classification considering multiple scattering between the targets. *J. Acoust. Soc. Am.*, 2004.

[13] Songming Hou, Knut Solna, and Hongkai Zhao. Imaging of location and geometry for extended targets using the response matrix. *Journal of Computational Physics*, 2004.

[14] E. Kerbrat, C. Prada, D. Cassereau, and M. Fink. Ultrasonic nondestructive testing of scattering media using the decomposition of the time reversal operator. *IEEE Trans. Ultrason., Ferroelec., Freq. Contr.*, 49(8), 2002.

[15] E. Kerbrat, C. Prada, and M. Fink. Imaging in the presence of grain noise using the decomposition of the time reversal operator. *Journal of the Acoustical Society of America*, 113(3):1230–1240, March 2003.

[16] A. Kirsch. Charactorization of the shape of a scattering obstacle using the spactral data of the far-field operator. *Inverse Problems*, 1998.

[17] A. Kirsch. The music algorithm and the factorization method in inverse scattering theory for inhomogenious media. *Inverse Problems*, 2002.

[18] R. Luke. Image synthesis for inverse obstacle scattering using the eigenfunction expansion theorem. *Computing*, 2005.

[19] J.-G. Minonzio, C. Prada, D. Chambers, D. Clorennec, and M. Fink. Characterization of subwavelength elastic cylinders with the decomposition of the time-reversal operator: Theory and experiment. *J. Acoust. Soc. Am.*, 117:789–798, 2005.

[20] G. Montaldo, M. Tanter, and M. Fink. Real time inverse filter focusing by iterative time reversal. *J. Acoust. Soc. Am.*, 115:768–775, 2004.

[21] G. Montaldo, M. Tanter, and M. Fink. Revisiting iterative time reversal processing: Application to detection of multiple targets. *J. Acoust. Soc. Am.*, 115:776–784, 2004.

[22] Claire Prada, Sebastian Manneville, Dimitri Spoliansky, and Mathias Fink. Decomposition of the time reversal operator: Detection and selective focusing on two scatterers. *Journal of the Acoustical Society of America*, 99:2067–2076, 1996.

[23] Claire Prada and Jean-Louis Thomas. Experimental subwavelength localization of scatterers by decomposition of the time reversal operator interpreted as a covariance matrix. *Journal of the Acoustical Society of America*, 114(1):235–243, 2003.

[24] Claire Prada, Jean-Louis Thomas, and Mathias Fink. The iterative time reversal process: Analysis of the convergence. *Journal of the Acoustical Society of America*, 97(1):62–71, 1995.

[25] R. O. Schmidt. Multiple emitter location and signal parameter estimation. *IEEE Trans. Antennas Propagation.*, 1986.

[26] M. Tanter, J.-L. Thomas, and M. Fink. Time reversal and the inverse filter. *J. Acoust. Soc. Am.*, 108:223–234, 2000.

[27] Hongkai Zhao. Analysis of the response matrix for an extended target. *SIAM Applied Mathematics*, 2004.